Environmental Science Nano

Defining silica-water interfacial chemistry under nanoconfinement using lanthanides

Journal:	*Environmental Science: Nano*
Manuscript ID	EN-ART-09-2020-000971.R1
Article Type:	Paper

Defining silica-water interfacial chemistry under nanoconfinement using lanthanides

Anastasia G. Ilgen*[1], Nadine Kabengi[2], Kevin Leung[1], Poorandokht Ilani-Kashkouli[2], Andrew W. Knight[3], and Lourdes Loera[1]

1. Sandia National Laboratories, Geochemistry Department, PO Box 5800 Mailstop 0754, Albuquerque, NM 87185-0754, United States
2. Department of Geosciences, Georgia State University, Atlanta, GA, United States
3. Sandia National Laboratories, Storage and Transportation Technologies Department, PO Box 5800 Mailstop 0754, Albuquerque, NM 87185-0754, United States

*Corresponding author. E-mail agilgen@sandia.gov

Environmental Significance Statement

The findings reported in this paper enable more accurate modeling for the fate and transport of contaminants, nutrients, and valuable chemical species, by taking into account nanoconfinement-driven changes to the energetics and products of interfacial reactions. Nanoconfined silica-water interfaces are pervasive in the environment, including nanopores in soils and in sedimentary silicate rocks. The reactivity of nanoconfined silica-water interfaces is hard to predict, compared to non-confined systems, due to the decrease in the dielectric constant and density of nanoconfined water across the pores. To quantify nanoconfinement-driven changes to silica-water interface reactivity we use lanthanide ions and their predictable variations in size, coordination environment, and hydration energies. We discovered that nanoconfinement promotes inner-sphere complexation and the formation of poly-nuclear surface species, and, as a result, changes the adsorption reaction from an endo- to an exothermic process. We report that ion's free energy of hydration is a descriptor that can be used in thermodynamic models to capture the nanoconfinement-driven changes in the equilibrium constant for inner-sphere adsorption reactions.

Defining silica-water interfacial chemistry under nanoconfinement using lanthanides

Anastasia G. Ilgen*[1], Nadine Kabengi[2], Kevin Leung[1], Poorandokht Ilani-Kashkouli[2], Andrew W. Knight[3], and Lourdes Loera[1]

1. Sandia National Laboratories, Geochemistry Department, PO Box 5800 Mailstop 0754, Albuquerque, NM 87185-0754, United States
2. Department of Geosciences, Georgia State University, Atlanta, GA, United States
3. Sandia National Laboratories, Storage and Transportation Technologies Department, PO Box 5800 Mailstop 0754, Albuquerque, NM 87185-0754, United States

*Corresponding author. E-mail agilgen@sandia.gov

Abstract

A quarter of Earth's land surface is covered by porous sedimentary silicate rocks, so silica-water interfaces are critical to the fate and transport of chemical species on a global-scale. However, while the physiochemical properties of unconfined silica-water interfaces are understood reasonably well, these properties have proven to be unpredictable when the interface is confined in nanometer-scale pores within sedimentary rocks. For example, the existing theories struggle to quantitatively predict how the energetics of adsorption reactions and the coordination environment of adsorbed species shift due to nanoconfinement of an interface. Here, we utilized gradual and known variations in the properties of trivalent lanthanide ions to decipher the chemical interactions that cause the nanoconfinement effects on chemistry at the silica-water interfaces. We discovered that the lanthanide's free energy of hydration (ΔG_{hydr}) is a descriptor that can be used to predict the extent to which nanoconfinement will change the thermodynamics and products of interfacial reactions. We show that nanoconfinement promotes inner-sphere complexation between lanthanides and silica surface, as well as the formation of polymeric surface species. In nanoconfined domains lanthanide's ΔG_{hydr} becomes less negative, reducing the energy required to dehydrate the ion during the formation of an inner-sphere surface complex. These nanoconfinement effects on chemistry become more pronounced for ions with lower hydration free energies.

Keywords: nanoconfinement, silica, lanthanides, hydration free energy, adsorption

Introduction

Molecular-scale chemical reactions at solid-water interfaces in near-surface environments define the macroscale fate, transport, and global cycling of all chemical species. The rates and products of these reactions are determined by the reactivity of solid interfaces but also by whether the interface is spatially confined.[1, 2] While confinement at the nanoscale (nanoconfinement) can occur under a variety of conditions, H_2O trapped in nanoscale silica (SiO_2) pores are of particular interest to geochemists because they are the most pervasive interfaces on Earth.[3] Consequently, accurately predicting the behavior of these interfaces is crucial for a broad range of predictive models, from determining the potential pollution pathways for stored nuclear waste to the probable consequences of removing H_2O or oil from underground reservoirs. The physiochemical properties of unconfined SiO_2-H_2O interfaces, whose surface chemistry is driven by silanol (Si–OH) functional groups, are reasonably well known, but the physiochemical properties of the nanoconfined interfaces are much less predictable.[1, 2, 4-7] The impact of nanoconfinement on adsorption reactions is not fully understood for SiO_2-H_2O interfaces.[2, 8-11] Understanding these interactions is urgent because the fundamental nanoscale chemistry drives macroscopic chemical fluxes.[1, 2, 8] For example, in nanoporous channels, methane gas has anomalously high solubility.[12] Similarly, in nanotubes, bulk ion mobilities and diffusivities no longer apply,[13] and transport behavior is defined by ion size, ion solvated structure, and ion-nanostructure interactions.[14]

To date, research has focused on the fascinating changes in the properties of H_2O confined in SiO_2 pores under idealized laboratory conditions and in molecular dynamic simulations. [4, 6, 14-16] For example, scientists previously observed that, as nanoscale pore size decreases, the ratio of

structured H_2O (molecules with lower rotational freedom) to unstructured H_2O increases, due to increasing surface-to-volume ratio within the reactive domains.[17, 18] Therefore, nanoconfinement decreases the dielectric constant, density, surface tension, and freezing point of H_2O,[16, 19-22] because of the overlap of electrical double-layers within the nanoscale pores and corresponding re-structuring of water's hydrogen bonding networks.[20, 22] However, the nanoconfinement effects are also impacted by the density of the Si–OH functional groups, and this phenomenon is not well studied, even though the variables are complex. [9, 10, 23, 24] Consequently, there is no fully reliable predictor for the thermodynamic and structural shifts in surface complexation (adsorption) reactions that occur between Si–OH and adsorbing ions when SiO_2-H_2O interfaces are confined. The changing chemical properties of H_2O itself [5-7, 17, 22, 25] result in a decrease in the solvation energy of dissolved ions and an increase in the aqueous complexation,[8, 26 27, 28] affinity and surface speciation of ions adsorbed onto solid surfaces,[8, 10, 23, 29, 30] as well as changes to the diffusion properties, electron transfer, [31-33] and nucleation reactions.[34-39]

One notable study on small molecule interactions with SiO_2 surfaces shows that the guest-host interactions become stronger with decreasing pore diameter and increasing density of Si–OH functional groups.[24] Another study examined surface speciation of zinc Zn^{2+} adsorbed at nanoconfined SiO_2-H_2O interfaces, and found that the local coordination of Zn^{2+} changes from primarily tetrahedral to a mixture of tetrahedral and octahedral inside progressively smaller SiO_2 pores.[10] In our previous studies, we used copper (Cu^{2+}) to assess nanoconfinement effect on the energetics of adsorption and on coordination environment of adsorbed Cu^{2+} because this ion is a contaminant of concern and has sufficient affinity for SiO_2 surface (suitable for investigation using X-ray absorption fine structure (XAFS) spectroscopy).[9, 23] We found that nanoconfinement

of the SiO_2-H_2O interface leads to dramatic changes in the energetics of Cu^{2+} adsorption: the adsorption is *endothermic* for unconfined, and *exothermic* for confined SiO_2. We also found that nanoconfinement promotes the formation of poly-nuclear Cu^{2+} species on the SiO_2 surface. However, this study was limited because only Cu^{2+} ion was used to probe the reactivity of SiO_2-H_2O interfaces, and therefore a number of important variables, such as charge and size of the adsorbing ion and its hydration free energy (ΔG_{hydr}), were not investigated. Therefore, in this study we use Ln^{3+} ions to further quantify how nanoconfinement affects the relative reactivity of nanoconfined (porous) and unconfined (non-porous) SiO_2-H_2O interfaces, in particular what role does the ion size and ΔG_{hydr} play. Lanthanide (Ln^{3+}) series, which includes elements with atomic numbers from 57 (lanthanum, La) to 71 (lutetium, Lu) all have the same charge (3+) and slight, gradual variations in their sizes (1.250 Å for La^{3+} to 0.995 Å for Lu^{3+})[40], ΔG_{hydr} values, and hydration numbers (8 for La^{3+} to 9 for Lu^{3+}).[41] They also have reasonably high adsorption affinity for SiO_2 surface, making them a remarkable system to study the chemistry of nanoconfined SiO_2-H_2O interfaces.

We quantified the effects of nanoconfinement on the Ln^{3+} adsorption reaction (both the energetics of adsorption and the coordination environment) by assessing the subtle and systematic differences in the ionic radii, ΔG_{hydr} values, and hydration numbers. We then employed theoretical energetic calculations of the solvation and dimerization processes to further support our experimental conclusions. Batch adsorption, column flow calorimetry, XAFS spectroscopy and cluster-based density functional theory (DFT) calculations all show that the Ln^{3+} ion's ΔG_{hydr} determines the extent to which nanoconfinement changes the heat signature and the products of interfacial reactions at SiO_2-H_2O interfaces. This discovery can form the

basis for a predictive thermodynamic framework that explains the nanoconfinement-driven changes in interfacial chemistry at the abundant SiO_2-H_2O interfaces, at both the molecular and macroscales. Moreover, these chemical changes in the Ln^{3+} binding at nanoconfined SiO_2-H_2O interfaces make it possible to improve the separation approaches for Ln^{3+} series ions – a key technological hurdle of our time. [42]

Experimental

SiO_2 substrates and adsorption experiments

A series of experiments were performed to measure the uptake of the lanthanide (Ln^{3+}) ions neodymium (Nd^{3+}), europium (Eu^{3+}), terbium (Tb^{3+}), thulium (Tm^{3+}) and lutetium (Lu^{3+}) onto porous and non-porous SiO_2. All Ln^{3+}ions were in trivalent oxidation state. All experiments were conducted using: (1) commercially available SBA-15 series mesoporous SiO_2 (Sigma Aldrich) with a mean pore diameter of 7.0±0.3 nm and 4.4±0.1 nm, and surface areas of 661±5 $m^2\,g^{-1}$ and 580±13 $m^2\,g^{-1}$, respectively [23] (referred to as "porous SiO_2" throughout); and (2) non-porous fumed silica SiO_2 (Sigma Aldrich) with a surface area of 192 $m^2\,g^{-1}$.[9] Two types of adsorption experiments were performed: single adsorbate and competitive adsorbate (for which all five lanthanides were present simultaneously). The background electrolyte in all cases was 0.01M sodium chloride (NaCl). Milli-Q H_2O with a resistivity of 18 MΩ·cm was used for all stock solutions and experiments. Lanthanide ion (Ln^{3+}) stock solutions were prepared by diluting their nitrate salts $Ln(NO_3)_3$ in Milli-Q H_2O. Aqueous concentration was verified by inductively coupled plasma mass spectrometry (ICP-MS) analysis as described below.

For the single adsorbate experiments, 20±3 mg of SiO_2 was weighted into centrifuge vials, then Milli-Q H_2O and 1M NaCl were added, and samples were hydrated for a minimum of 48 hours. At the beginning of the adsorption experiment, Ln^{3+} stock solution was added, and the total volume of each sample was brought to 20 mL. The pH was immediately adjusted to pH 6.0±0.1 using dilute sodium hydroxide (NaOH) or hydrochloric acid (HCl), and samples were reacted for 48 hours, at which point equilibrium was reached. For the competitive adsorption experiment, 50±3 mg of SiO_2 was weighted into centrifuge vials, and milli-Q H_2O and NaCl were added to hydrate the substrate for a minimum of 48 hours. Stock solution containing 19 μM L^{-1} of Nd^{3+}, Eu^{3+}, Tb^{3+}, Tm^{3+} or Lu^{3+} were used, and the final concentrations for each Ln^{3+} in the reactors were set at 0.2, 1, 5, and 10 μM L^{-1}. The total volume of each reactor was 20 mL. Immediately thereafter, dilute NaOH or HCl was used to adjust the pH of each reactor to pH 6.0±0.1, and samples were equilibrated for 48 hours on a shaker table. All experiments were performed at ambient temperature (22 °C).

At the completion of the adsorption experiments, samples were centrifuged to separate solid and aqueous phases. The aqueous portion was filtered using a 0.2 μm nylon membrane filter and acidified using 6N ultrapure nitric acid (HNO_3). Aqueous samples were analyzed using ICP-MS to quantify the concentrations of each Ln^{3+} remaining in the aqueous phase after adsorption took place. ICP-MS data was acquired using a NexION 350D mass spectrometer (Perkin Elmer) equipped with a collision-reaction cell. The quantification of all Ln^{3+} concentrations was done in normal mode. Calibration curves for each analyte were obtained by running certified standard solutions prior to each analytical run, with a resulting R^2 value of 0.9999 or better.
From aqueous concentrations, surface coverage (uptake) in μmoles m^{-2} was calculated using:

$$Surface\ coverage = \frac{C_{initial} - C_{final}}{m_{SiO_2} \times SA_{SiO_2}}$$

Where $C_{initial}$ and C_{final} are Ln^{3+} concentrations in μmoles L^{-1} at the onset and at the completion of the adsorption experiment, respectively; m_{SiO_2} is mass in grams and SA_{SiO_2} is surface area in $m^2\ g^{-1}$ for SiO_2 solids.

X-ray absorption fine structure spectroscopy (XAFS) data collection and analysis

Samples for XAFS analysis were prepared by equilibrating aqueous suspensions of porous SiO_2 with 4.4 nm and 7.0 nm pores and non-porous fumed SiO_2 with the Nd^{3+}, Tb^{3+}, and Lu^{3+} stock solutions described above. The pH was adjusted to 5.8±0.1, and samples were suspended in 0.01 M NaCl background electrolyte.

XAFS data at the Nd^{3+}, Tb^{3+}, and $Lu^{3+}L_{III}$-edges was collected using beamline 10-BM at the Advanced Photon Source (APS), Argonne National Laboratory. The beamline is equipped with a water-cooled Si(111) monochromator, which was calibrated using metal reference foils and detuned by 50% to reject higher harmonics . The monochromator step size was 10 eV in the pre-edge, 0.5 eV in the XANES region, and 0.05 $Å^{-1}$ in the XAFS region. Fluorescent counts were collected using a Vortex Si Drift solid-state 4-element detector. Standard compounds analyzed included Nd_2O_3, Tb_2O_3, and Lu_2O_3.

The XAFS data processing was done using the Athena interface and XAFS data fitting was done using the Artemis interface [43] to the IFEFFIT [44] program. The background subtraction

(AUTOBK algorithm [45]), normalization, and conversion into k-space were conducted as described elsewhere.[46] The Fourier-transformed Nd, Tb, and Lu L_{III}-edge XAFS spectra were analyzed using the Artemis interface to IFEFFIT by fitting theoretical paths,[47] which were based on the structures of lanthanide-containing apatite.[48] The structure files were edited to remove partial occupancies, so that FEFF calculations could be performed. The fitting was done in R-space using a Hanning window and k-weights of 1, 2, and 3. The amplitude reduction factor (S_0) was determined by fitting XAFS spectra collected on Nd_2O_3, Tb_2O_3, and Lu_2O_3 standards. Due to higher noise associated with the Nd adsorption samples, only the 1st shell was fitted. The amplitude reduction factor S_0 was set at 0.88 for Nd, 0.67 for Tb, and 0.71 for Lu, based on fitting data collected on model compounds Nd_2O_3, Tb_2O_3, and Lu_2O_3. Errors at a 95% confidence level (2 sigma) are shown in parenthesis in SI Table S2.

Microcalorimetry experiments

The flow microcalorimeter (FMC) used in this study was custom-designed and fabricated in the Kabengi Laboratory at Georgia State University. The details about this instrumentation and basic operational procedures can be found in previous publications.[49] To obtain the thermal signatures and subsequently the heats of Nd^{3+}, Tb^{3+}, and Lu^{3+} adsorption, a 20.0 ± 0.5 mg sample of porous SiO_2 or 50.0 ± 0.5 mg of non-porous SiO_2 particles was homogeneously packed into the sample holder of the FMC's microcolumn. The packed column was equilibrated with a 0.01 M $NaNO_3$ solution at a flow rate of 0.30 ± 0.03 mL min^{-1} until thermal equilibrium was reached, as indicated by a steady baseline. A fixed mass of Ln^{3+} was injected onto the column with a controlled volume of $Ln(NO_3)_3$ stock solution. For porous SiO_2 experiments, the concentrations were 7.86 μM for $Nd(NO_3)_3$, 11.22 μM for $Tb(NO_3)_3$ and 8.42 μM for $Lu(NO_3)_3$. Due to the low

calorimetric signal obtained for non-porous SiO_2, the concentrations of the stock solutions were increased to 157.2 μM for $Nd(NO_3)_3$, 224.4 μM for $Tb(NO_3)_3$, and 168.4 μM for $Lu(NO_3)_3$. To keep the ionic strength (I) constant throughout the experiment, the $NaNO_3$ concentration was kept at 0.01 M. The calorimetric signal corresponding to the interaction of Ln^{3+} with the SiO_2 sample was thus obtained. Once the thermal signal returned to the original baseline, the input solution was switched back to 0.01 M $NaNO_3$. Effluent samples were collected during the experiment for quantifying aqueous concentrations of Ln^{3+} using ICP-MS as described above. Aqueous samples for ICP-MS analysis were collected during flow experiment and preserved with 6N ultrapure HNO_3. The mass of Ln^{3+} retained at (and subsequently desorbed from) the surface was determined by a mass balance calculation between the mass of the injected Ln^{3+} and the mass recovered in all effluents. The heats of reactions (Q_{ads} in $mJ \cdot m^{-2}$) and molar enthalpies (ΔH in $kJ \cdot mol^{-1}$) were calculated by integrating the calorimetric peaks and were converted to energy units (Joules) by calibration with calorimetric peaks of known energy inputs generated from a calibrating resistor. The solution pH was adjusted daily using dropwise addition of 0.1 M HNO_3 and 0.1 M NaOH to achieve a final pH of 6.0 ± 0.1. Changes in total concentration and ionic strength resulting from pH adjustments were determined to be negligible.

Density Functional Theory Calculations

Cluster-based density functional theory (DFT) calculations with varying dielectric constants were performed to estimate how ΔG_{hydr} of Lu^{3+} and Nd^{3+} changes as a function of the dielectric constant of H_2O. The free energy of dimerization reactions for Nd^{3+} and Lu^{3+} were calculated in pure H_2O using Gaussian code g09,[50] with explicit H_2O and the PCM dielectric solvation method,[51] and the Stuttgart 1993 ("cep-121g") effective core potential.[52] For Ln^{3+} monomers in

H_2O, 8- and 9-coordinated solvation shells were the most stable for Lu^{3+} and Nd^{3+} at both ε=10 and ε=78. Two dimer clusters were considered, having overall nominal stoichiometries of $(Ln^{3+})_2(OH^-)_2(H_2O)_n$, with n=12 and 13, and the "OH^-" groups bridging the cations. The latter structure was found to be more stable, and therefore was used in all cases. Note that the optimized dimer structures for Lu^{3+} and Nd^{3+} differ in their bridge structures. For Lu^{3+}, the bridging groups are in effect two $H_3O_2^-$, while for Nd^{3+} they consist of one $H_3O_2^-$ and an OH^-.

Results and Discussion

Adsorption of lanthanides onto porous and non-porous SiO_2 surfaces

Batch experiments were performed for single Ln^{3+} ions (where only Nd^{3+}, Eu^{3+}, Tb^{3+}, Tm^{3+} or Lu^{3+} were present) and in competitive adsorption studies (with all five Ln^{3+} ions present simultaneously). Systematic variation in the adsorption affinity on the examined SiO_2 surfaces was observed, specifically that the uptake of individual Ln^{3+} ions increases at higher atomic numbers (Figure 1a-b), in agreement with earlier investigations.[53] To assess how nanoconfinement within SiO_2 affects adsorption trends, comparisons were made between the surface-area-normalized Ln^{3+} uptake on porous SiO_2, with mean pore diameters of 4.4 nm and 7.0 nm, respectively. As in our previous study of Cu^{2+},[9] pore-diameter-dependent adsorption was observed for the lighter (larger) Ln^{3+} ions (Nd^{3+}, Eu^{3+}, and Tb^{3+}); however, the heavier (smaller) Ln^{3+} ions (Tm^{3+} and Lu^{3+}) did not exhibit pore diameter dependence (Figure 1c-f).

Our previous research indicates that slight re-structuring of H-bonding networks in H_2O confined in SiO_2 pores results in a decrease in the freezing temperature and density of H_2O, [54] and we deduce that similar re-structuring of H_2O inside the pores is likely to affect the local structure

around the adsorbing Ln^{3+} ions. Therefore, *here we hypothesize that nanoconfinement effects are more pronounced in weaker-hydrated ions than in ions with tighter hydration spheres and higher free energy of hydration (ΔG_{hydr}).* The reported ΔG_{hydr} values increase from -3280 kJ·mol^{-1} for Nd^{3+} to -3515 kJ·mol^{-1} for Lu^{3+},[40, 41] and our calculated values listed in the SI file are -3454 kJ·mol^{-1} for Nd^{3+} and -3629 kJ·mol^{-1} for Lu^{3+}. The batch adsorption results support our hypothesis since adsorption of strongly hydrated Tm^{3+} and Lu^{3+} is independent of pore diameter (Figure 1e,f). *We therefore conclude that the main chemical descriptor determining whether nanoconfinement affects the adsorption behavior is the ΔG_{hydr} of the adsorbing ion.* As hydration numbers decrease and negative hydration free energy increases, dehydration reactions become more energetically costly, so the nanoconfinement effects on adsorption become less pronounced as the Ln series progresses from Nd^{3+} to Lu^{3+}. Our previous work on Cu^{2+} could also support this conclusion, since Cu^{2+} exhibits pore-diameter-dependent adsorption on the same SiO_2 materials and has the hydration energy lower than the examined Ln^{3+} ions (-506.75 kcal·mol^{-1} or -2120 kJ·mol^{-1}).[23, 55]

The competitive adsorption results agree with the single-element tests, showing that heavier (smaller) Ln^{3+} ions have higher affinity for SiO_2 surfaces (Figure 2a-c). Interestingly, the slope in the uptake *vs*. ionic radius plot of the Ln^{3+} ions becomes steeper with increasing surface coverage, indicating that the difference in affinities between lighter and heavier Ln^{3+} ions depends primarily on the surface coverage (uptake) (Figure 2a-c). Consequently, the surfaces of both non-porous and porous SiO_2 solids become progressively more selective towards heavier Ln^{3+} ions, as increasing coverage results in increasing competition for the adsorption sites. Consequently, as more porous SiO_2 surface sites are occupied, the task of separating individual

Ln^{3+} ions from each other using column or batch separation becomes increasingly efficient. The overall Ln^{3+} uptake was higher for non-porous SiO_2, likely because adsorption of Ln^{3+} onto porous SiO_2 is hindered by slow diffusion into the long channels in porous SiO_2 (Supporting Information, Figure S1). In the competitive adsorption study, the pH values for porous SiO_2 samples with the highest concentrations of Ln^{3+} ions decreased from an initial pH of 6.0 to a pH of 5.6 or 5.7. However, under the same Ln^{3+} adsorption conditions, the pH in non-porous SiO_2 samples remained constant at a pH of 6.0. These pH trends may indicate that, during Ln^{3+} adsorption onto porous SiO_2, inner-sphere complexation reactions cause the SiO_2 surface to de-protonate. In contrast, the predominant mode of adsorption for non-porous SiO_2 is outer-sphere complexation, where Ln^{3+} ions do not displace protons from the surface, as indicated by the lack of change in pH.

To further elucidate the mechanism of surface complexation reactions, the equilibrium constants of the reactions for porous and non-porous SiO_2 solids were assessed. The reactive sites on the SiO_2 surfaces are the silanol functional groups Si–OH. The surface-site density of silanol groups is 2.3 ± 0.2 OH nm^{-2} for the porous SiO_2 with 4.4 nm pores, 1.8 ± 0.2 OH nm^{-2} for the porous SiO_2 with 7.0 nm pores,[54] and 2.15± 0.2 OH nm^{-2} for non-porous SiO_2.[9] The hydroxyl site densities are similar for the porous and non-porous SiO_2 solids; however, a different concentration of surface Si–OH groups was available in each reactor, since the constant was the mass of the solid (50 mg) rather than the surface area (661±5 m^2 g^{-1} for 7.0 nm, 580±13 m^2 g^{-1} for 4.0 nm, and 192 m^2 g^{-1} for non-porous SiO_2 [54,9]). The equilibrium constant for the surface complexation reaction was calculated using:

$$K_{ads} = \frac{[Ln^{3+}_{ads}] \times [H^+]}{[Si-OH_{surf}]},$$

where $[Ln^{3+}_{ads}]$ in moles·m^{-2} is the concentration of adsorbed Ln^{3+}, $[H^+]$ in moles·L^{-1} is the proton concentration at the completion of the experiment, and $[Si-OH_{surf}]$ in moles·L^{-1} is the concentration of available hydroxyl surface sites available in the reactor. The calculated K_{ads} values are shown in Figure 2d-f, and the summary table with these values is included in the SI file (Table S2). Plotted against the surface coverage by Ln^{3+} ions, these K_{ads} values elucidate the differences between the chemical adsorption mechanisms for porous and non-porous SiO_2. For

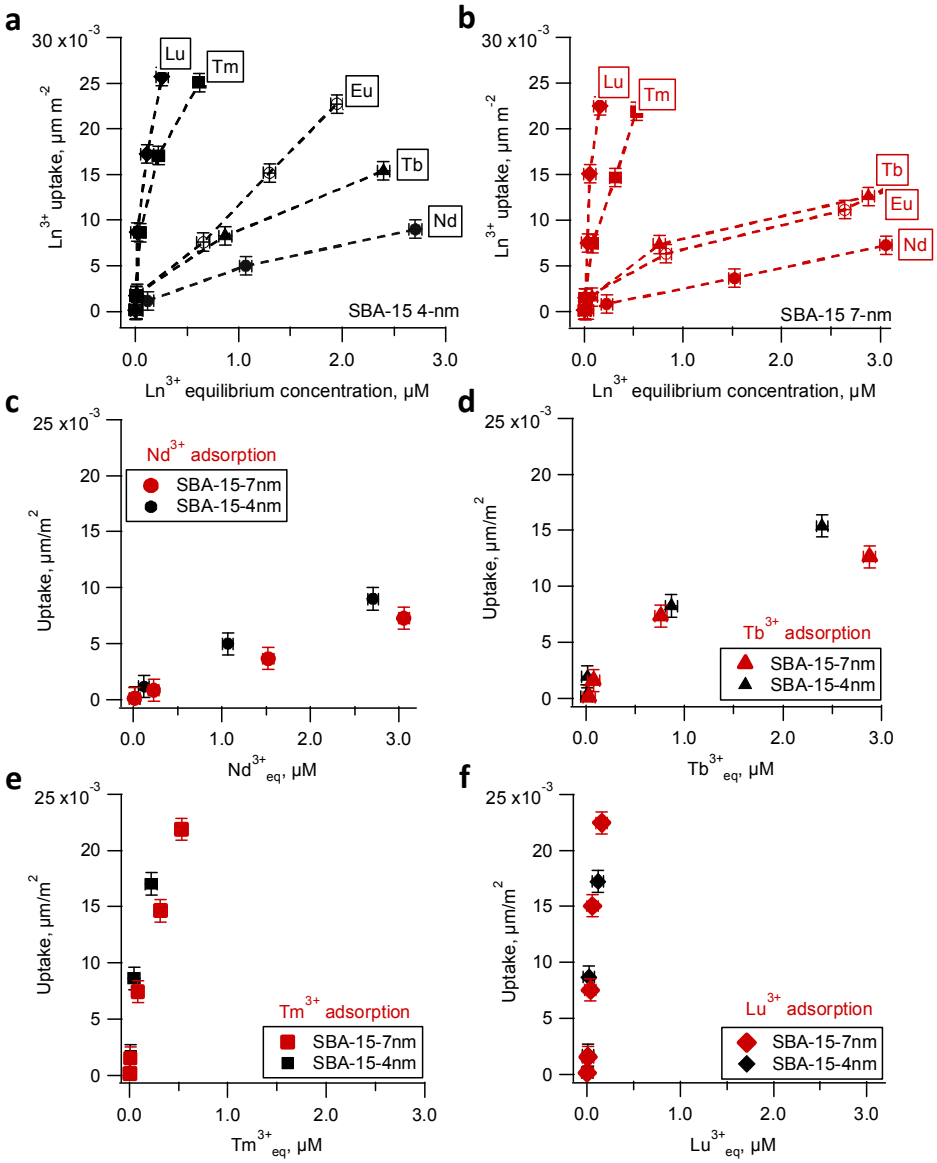

Figure 1. Mass-dependent uptake of individual Ln^{3+} ions onto porous SiO_2 with (a) 4.4 nm pores, and (b) 7.0 nm pores. Comparison of the uptake on 4.4 nm pores and 7.0 nm pores is shown for (c) Nd^{3+}, (d) Tb^{3+}, (e) Tm^{3+}, and (f) Lu^{3+}. For the lighter Ln^{3+} ions (Nd^{3+}, Tb^{3+}, and Eu^{3+}) the uptakes are higher on SiO_2 surfaces with 4.4 nm pores than on surfaces with 7.0 nm pores. For the heavier Tm^{3+} and Lu^{3+} ions, the uptakes are independent of the pore diameter.

non-porous SiO_2, the plot gradually collapses into a single line; however, for porous SiO_2, the relationship is non-linear (Figure 2d-f).

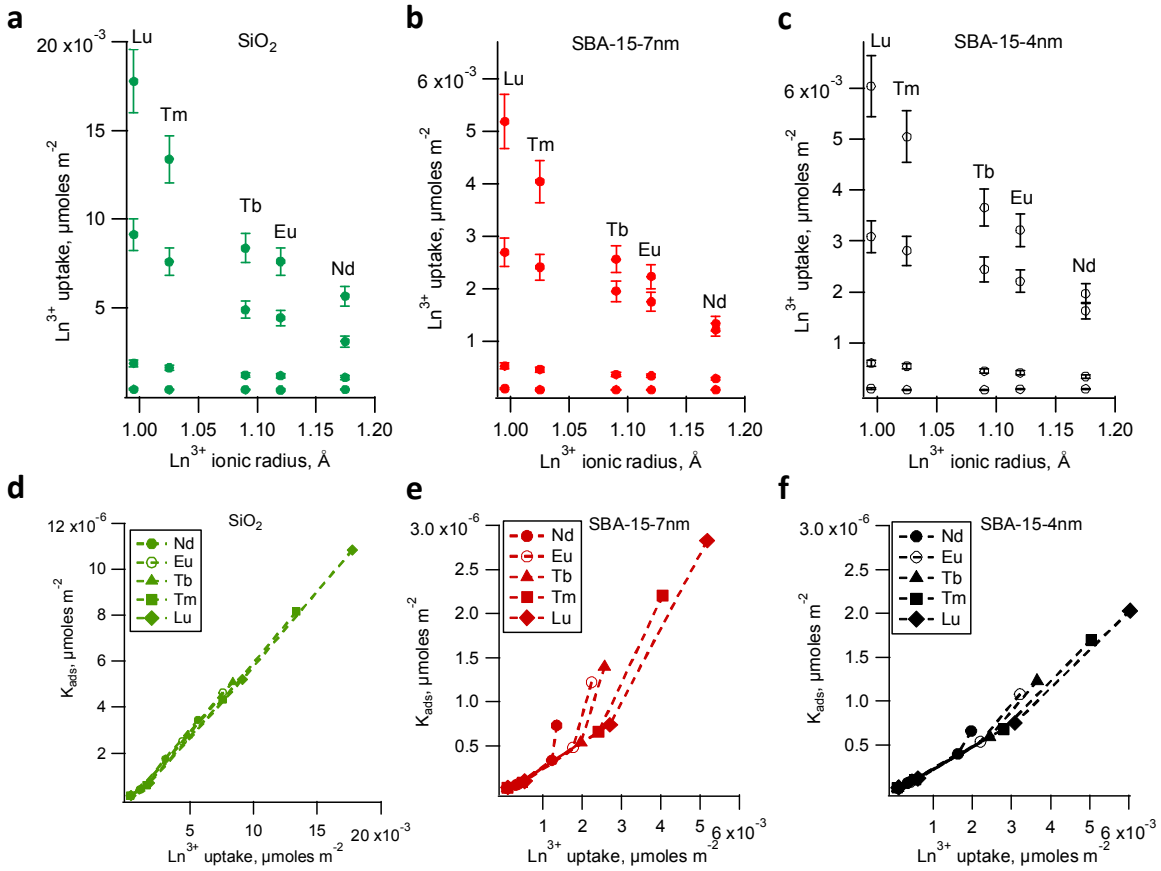

Figure 2. Competitive adsorption of lanthanides onto (a) non-porous SiO_2 and porous SiO_2 solids with (b) 4.4 nm and (c) 7.0 nm pores. The slope of uptake *vs*. ionic radius becomes steeper for the higher surface loadings, indicating increasing competition for surface adsorption sites. Equilibrium constant for adsorption reaction K_{ads} plotted *vs*. Ln^{3+} uptake for (d) non-porous SiO_2 and porous SiO_2 solids with (e) 4.4 nm and (f) 7.0 nm pores.

Bulk adsorption experiments (pH shifts and K_{ads} values) indicate that adsorption mechanism differs when porous and non-porous SiO_2 are compared. This conclusion was further validated by the XAFS and microcalorimetry measurements, and DFT calculations discussed below.

Local coordination environment of adsorbed lanthanides

The local coordination environment around Nd^{3+}, Tb^{3+}, and Lu^{3+} adsorbed onto non-porous and porous SiO_2 solids was characterized using XAFS. As anticipated, the XAFS data shows that the nanoconfinement affects the local coordination environment of adsorbed species. However, surprisingly, the nanoconfinement effects proved to be similar for all examined Ln^{3+} ions, regardless of mass (XAFS fitting parameters are shown in SI Table S2).

The XAFS analysis was performed on both the 1st and 2nd shell nearest-neighbors to assess the nanoconfinement effects. However, only the 1st shell Nd–O spectral feature was fit for Nd^{3+}, due to poor signal-to-noise ratio. The 1st shell Nd–O spectral feature was fit with one Nd–O backscattering path at 2.50 Å for non-porous SiO_2, and at 2.54-2.56 Å for Nd^{3+} adsorbed onto porous SiO_2 with 7.0 nm and 4.4 nm pores (Table S2). The Nd–O distances become slightly longer (by 0.04-0.06 Å) under nanoconfinement, which shows that first shell hydration sphere around adsorbed Ln^{3+} may be "relaxing" under nanoconfinement.

For Tb^{3+} and Lu^{3+}, the improved signal-to-noise ratios allowed for the examination of 2nd shell features. The 1st Tb–O shell was fit with two Tb–O backscattering paths at 2.22-2.28 Å and at 2.42 Å (Table S2). The presence of the Tb–Si backscattering feature indicates that Tb^{3+} forms inner-sphere adsorption complexes (consistent with our batch adsorption pH trends) on the examined porous SiO_2 solids, where the Tb–Si distance is consistent with a bi-dentate bi-nuclear complex geometry (Tb–Si is 3.41-3.66 Å). With decreasing pore diameter, the Tb–O increases slightly, from 2.22 Å for SiO_2 with 7.0 nm pores to 2.28 Å for SiO_2 with 4.4 nm pores. For both pore diameters, the presence of Tb–Tb backscattering suggests that some of the adsorbed Tb^{3+}

forms dimers or other type of polymer species on the SiO_2 surface, and the Tb–Tb distance of 3.64-3.75 Å further suggests that the terbium dimers exist as edge-sharing moieties (*e.g.*, as in the structure of xenotime [56]). This indicates that nanoconfinement may promote the formation of poly-nuclear (*e.g.*, dimer) Ln^{3+} species on SiO_2 surface.

For Lu^{3+} adsorption samples prepared at pH 6.0, the optimum fit for the Lu–O 1st shell was achieved by using two Lu–O backscattering paths at 2.13-2.17 Å and at 2.31-2.35 Å. Again, decreasing pore diameter results in a subtle elongation of the mean Lu–O distance. The 2nd shell was fit with Ln–Si backscattering path at 3.33-3.63 Å and (like Tb^{3+}), reflects a bi-dentate bi-nuclear adsorption complex with backscattering features that indicate that some of the adsorbed Lu^{3+} formed dimer or other type of polymer surface species. The resulting Lu–Lu distances were 3.81-3.93 Å, indicating a single link between Lu^{3+} polyhedra (an edge sharing, or 2 links would

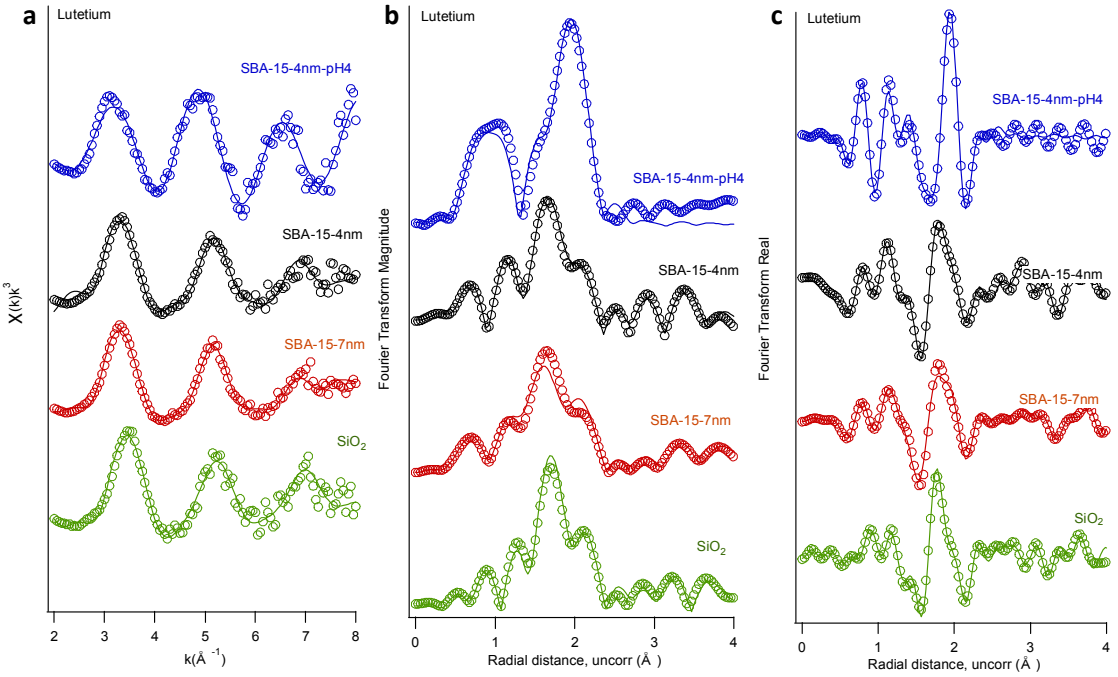

Figure 3. X-ray absorption fine structure (XAFS) spectroscopy data and shell-by-shell fitting results for Lu^{3+} adsorbed onto non-porous silica (SiO_2) and porous SiO_2 with 4.4 nm pores (SBA-15-4nm) and with 7.0 nm pores (SBA-15-7nm). (a) XAFS data and fits shown in k-space, (b) magnitude of the Fourier transform, and (c) the real part of Fourier transform. The markers denote the experimental data and the lines are the fits.

occur around 3.55 Å, as reported for keiviite in Yakubovich, *et al.* [57]). The XAFS data and fits for Lu^{3+} are shown in Figure 3.

The pH effects were also tested on Lu^{3+}, which was chosen due to its high affinity for the SiO_2 surface (the uptake of all Ln^{3+} is lower at pH 4.0 than pH 6.0), consistent with adsorption edge

data for cations).[58] Importantly, the coordination environment of adsorbed Lu^{3+} proved to be quite different between samples prepared at pH 6.0 and at pH 4.0 (Table S2). The porous SiO_2 sample prepared with 4.4 nm pores at pH 4.0 showed lower surface loading and a worse signal-to-noise ratio than the sample prepared at pH 6.0. Consequently, only the 1st shell Lu–O distance in this sample was fit, and the fit required two Lu–O backscattering paths. The results confirmed significantly longer Lu–O distances for the pH 4.0 sample (2.27 and 2.39 Å) than for the pH 6.0 sample (2.17 and 2.35 Å), presumably due to changes in the deprotonation state of H_2O/OH^- in the 1st shell of Lu^{3+}. At pH 4.0, more H_2O molecules around the Lu^{3+} are in the fully protonated state (H_2O), while at pH 6.0 some of these molecules de-protonate to OH^-. Given their respective electrostatic considerations, the Lu–OH^- distance should be shorter than the Lu–H_2O distance. For example, in the Lu^{3+} dimer calculation, the two Lu^{3+} are linked by two $H_5O_2^+$ "bridges," which can be regarded as a mix of OH^- and H_2O. The distance between Lu^{3+} and the O atoms in these OH^--containing bridges are 2.19, 2.26, 2.33, and 2.38 Å (average 2.29 Å), while the Lu^{3+}–O_{water} distances are more uniform and range from 2.30 to 2.38 Å (averaging 2.35 Å).

Heats of adsorption measured with flow microcalorimetry

Flow microcalorimetry was performed to quantify heats of reaction on non-porous and porous SiO_2 solids during Ln^{3+} adsorption. These heat measurements indicate mass-dependent and pore-size-dependent adsorption of Nd^{3+}, Tb^{3+}, and Lu^{3+} onto non-porous and porous SiO_2 surfaces. For all three Ln^{3+} ions, the flow microcalorimetry notably indicates a reverse in the sign of the calorimetric signal, showing an *exothermic* signal on SiO_2 with 4.4 nm and 7.0 nm pores and *endothermic* signal for non-porous SiO_2 (Figure 4). This finding is consistent with our earlier report for Cu^{2+} adsorption onto the same SiO_2 substrates, evaluated using the same experimental

setup.[9] The summary of microcalorimetry measurement results and surface coverages is shown in SI (Table S3). For Nd^{3+}, Tb^{3+} and Lu^{3+}, the molar enthalpies of adsorption ΔH_{ads} on porous SiO_2 solids are significantly more energetic (*exothermic*, more negative) than on non-porous SiO_2 (*endothermic*, less negative). Additionally, as the pore diameter decreases from 7.0 nm to 4.4 nm, Nd^{3+} shows the largest change in the adsorption enthalpy (increase from -69.565 $kJ \cdot mol^{-1}$ to -87.270 $kJ \cdot mol^{-1}$), which indicates that the energetics of adsorption for the lighter lanthanides are more strongly affected by nanoconfinement, further validating the batch adsorption results (Figure 1c-f). In the microcalorimetry set of experiments, the Ln^{3+} eluent concentrations were chosen to correspond to the higher end of the surface coverages observed in the batch adsorption experiments, although kinetic constraints in the flow systems prevent the achievement of full adsorption equilibrium. The flow microcalorimetry experiments on non-porous SiO_2 had to be conducted at a higher Ln^{3+} eluent concentration to achieve a detectable calorimetric signal. Because of this adjustment in the experimental design, higher Ln^{3+} surface coverages were achieved for non-porous SiO_2 than either of the porous SiO_2 solids (Table S3). Surface coverage is an important variable in flow microcalorimetry measurements, since solid surfaces commonly have more than one type of reactive site. Adsorption onto high-energy sites, which are occupied first, will result in a more energetic calorimetric signal, compared to lower-energy surface sites. Therefore, ΔH_{ads} values can only be compared for similar surface coverages (Ln^{3+} uptakes).

The reverse in the calorimetric signal from *endo-* to *exothermic* between non-porous and porous SiO_2 solids could be explained by four possible mechanisms. First, the predominant adsorption mechanism may be inner-sphere complexation for porous SiO_2 and outer-sphere complexation for non-porous SiO_2, as supported by the pH measurements in the bulk adsorption experiments

(which offer evidence of surface de-protonation reactions only for porous SiO_2 solids) and the XAFS data (which shows stronger Lu-Si backscattering for porous SiO_2). Literature reports similar effects for muscovite surfaces (for which the adsorption free energy ΔG_{ads} is more negative when the ion forms an inner-sphere complex [59]) and zeolites (which demonstrate enhancement of inner-sphere complexation for major cations, specifically Na^+, K^+, and Ca^{2+} [11]). Second, the formation of polymeric Ln^{3+} species only on the surfaces of porous SiO_2 solids could cause an *exothermic* reaction. For Ln^{3+} to form a dimer, one or two H_2O molecules must be removed from the Ln^{3+} hydration sphere; followed by the proton release and the formation of a new $Ln^{3+}-(OH^-)-Ln^{3+}$ bond (Table 1), which are, cumulatively, an *exothermic* process. The Ln^{3+} dimerization on the SiO_2 surface may be more prevalent for porous SiO_2, as indicated by the slightly higher Lu–Lu backscattering amplitude in porous SiO_2 (CN column in Table S2). Third, due to nanoconfinement, H_2O inside SiO_2 pores has altered local structure, causing changes in the local hydration structure around Ln^{3+} ions approaching SiO_2 surface. This re-structuring of H_2O molecules is expected to change the ΔG_{hydr}, and therefore the overall energetics of the adsorption reaction. Based on the calculated and measured thermodynamic values, we anticipate that these three mechanisms are acting simultaneously. Fourth, the surface coverages achieved by Ln^{3+} ions for porous SiO_2 solids are lower (Table S3), compared to non-porous SiO_2, so high-energy adsorption sites are occupied first, which likely leads to higher heat signature.[60] We postulate, however, that this difference in surface coverages plays a secondary role, because Cu^{2+} surface coverages in our earlier work on porous and non-porous SiO_2 were similar, and yet we saw the same switch from *endo-* to *exothermic* process when non-porous and porous SiO_2 were compared.[9]

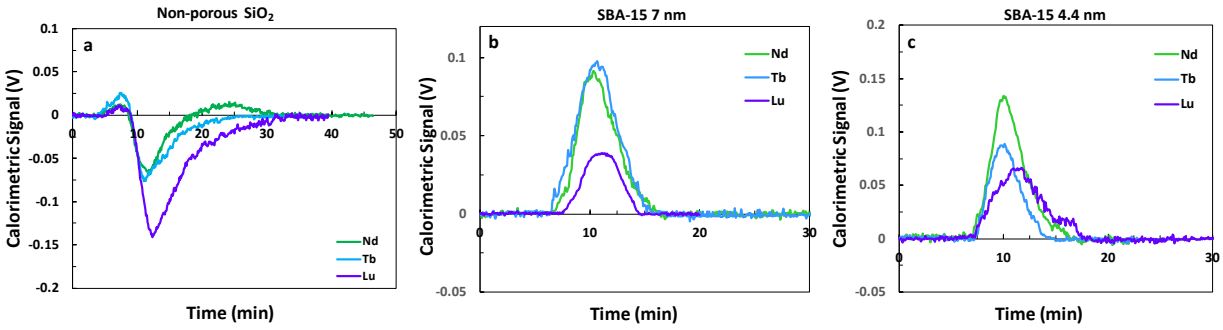

Figure 4. Total heats of adsorption for Nd^{3+}, Tb^{3+} and Lu^{3+} (a) for non-porous SiO_2; (b) for porous SiO_2 with 4.4 nm pores; and (c) for porous SiO_2 with 7.0 nm pores. For concentration-normalized data see Table S3.

Energy considerations for lanthanide adsorption at nanoconfined SiO_2 surfaces

To further test the validity of the second and third proposed mechanisms (Ln^{3+} dimerization and ΔG_{hydr} change under nanoconfinement), density functional theory calculations were performed for Nd^{3+} and Lu^{3+} in pure H_2O (Figure 5). An H_2O value for dielectric constant (ε) of ε = 78 was used for the unconfined (bulk) water calculations. To approximate the nanoconfinement effect, the ε of H_2O was lowered to ε = 10 for the confined calculations. [17] The results are summarized in Table 1. Note that the "H^+" free energies and enthalpies, only, relevant to dimerization due to proton release, are calculated using a B3LYP/6-311+G(d,p) level of theory[61] instead of the BP86 functional widely used to model Ln^{3+} hydration. The reason is that the B3LYP method yields proton hydration free energies in good agreement with measurements, while the BP86 functional significantly overestimate H^+ stabilization in water.

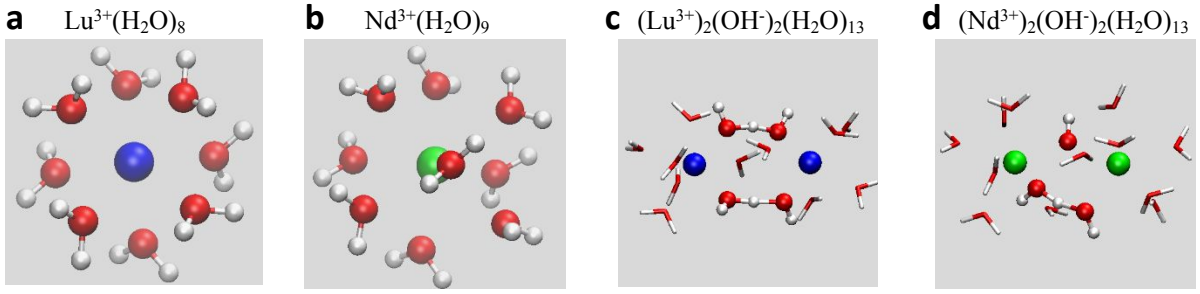

Figure 5. Schematic of (a) Lu^{3+} monomer with 8 neighboring H_2Os; (b) Nd^{3+} monomers with 9 neighboring H_2Os; (c) Lu^{3+} dimer; (d) Nd^{3+} dimer. In (c) and (d), only the negatively charged bridging groups are shown as ball-and-stack models; the other H_2O molecules are depicted as stick figures. These systems (c and d) were used to assess the free energy of the dimerization reaction.

Our calculations further support the postulated effect of dimerization reactions on the calorimetric data. The Gaussian calculations show that dimerization is favorable for Lu^{3+} in bulk liquid H_2O (ε=78), but not for Nd^{3+}. As ε decreases (due to nanoconfinement), the favorability of dimerization for Lu^{3+}increases (Table 1). These results support the hypothesis that a reverse in the calorimetric signal could be caused by the increased formation of polymeric Lu^{3+} species on the surfaces of porous SiO_2 solids. Nd^{3+} dimerization favorability in bulk water is not predicted to be strongly affected by lowering the dielectric constant. However, the SiO_2 surface was not explicitly included in this analysis, and it is possible that other plausible H_2O configurations would alter the calculations. Even so, the structural difference in the hydrated Lu^{3+} and Nd^{3+} dimer structures are readily reproducible (*e.g.* in the Fig. 5d structure, if Nd^{3+} is replaced with Lu^{3+}, and structure is re-optimized, then the configuration recovers, as in Fig. 5c).

Table 1. Calculated free energies of dimerization for Nd^{3+} and Lu^{3+} in pure H_2O with a dielectric constant (ε) of 78, and in pure H_2O with an ε of 10 (nanoconfinement conditions). The stoichiometry of assumed reactions is shown.

Nd^{3+}, ε = 78		
H_2O + Nd(III) $(H_2O)_8 \rightarrow$ Nd(III) $(H_2O)_9$	ΔG = -0.03 eV	ΔG = -2.99 kJ/mol
2Nd(III) $(H_2O)_9 \rightarrow$ $3H_2O$ + 2 "H^{+}" +Nd(III)$_2$ $(OH^{-})_2$ $(H_2O)_{13}$	ΔG = 0.48 eV at pH=6, [Nd]=10^{-5} M	ΔG =+46.08 kJ/mol ΔE = +85.74 kJ/mol
Nd^{3+}, ε = 10		
H_2O + Nd(III) $(H_2O)_8 \rightarrow$ Nd(III) $(H_2O)_9$	ΔG = -0.13 eV	ΔG = -12.80 kJ/mol
2Nd(III) $(H_2O)_9 \rightarrow$ 3H2O + 2 "H^{+}" + Nd(III)$_2$ $(OH^{-})_2$ $(H_2O)_{13}$	ΔG = 0.48 eV at pH=6, [Nd]=10^{-5} M	ΔG = +46.43 kJ/mol ΔE = -1.46 kJ/mol
Lu^{3+}, ε = 78		
H_2O + Lu(III) $(H_2O)_8 \rightarrow$ Lu(III) $(H_2O)_9$	ΔG= +0.03 eV	ΔG =2.89 kJ/mol
2Lu(III) $(H_2O)_8 \rightarrow$ H_2O + 2 "H^{+}" + Lu(III)$_2$ $(OH^{-})_2$ $(H_2O)_{13}$	ΔG = -0.25 eV at pH=6, [Lu]=10^{-5} M	ΔG = -23.87 kJ/mol ΔE = +20.30 kJ/mol
Lu^{3+}, ε = 10		
H_2O + Lu(III) $(H_2O)_8 \rightarrow$ Lu(III) $(H_2O)_9$	ΔG = +0.02 eV	ΔG =1.93 kJ/mol
2Lu(III) $(H_2O)_8 \rightarrow$ H_2O + 2 "H^{+}" + Lu(III)$_2$ $(OH^{-})_2$ $(H_2O)_{13}$	ΔG = -0.39 eV at pH=6, [Lu]=10^{-5} M	ΔG = -37.35 kJ/mol ΔE = -47.48 kJ/mol

Notes:

"H^+" denotes $H_5O_2^+$ as in Grabowski et al., 2002.[48]
ΔE denotes the net energy of reaction.
ΔG was calculated at pH=6 and Ln^{3+} concentration of 10^{-5} M to explore the same conditions as in the experiments.

In addition to the free energies shown in Table 1, the solvation energies of single Ln^{3+} ions in H_2O were calculated for different dielectric constants. In agreement with the literature, the Nd^{3+} ions were coordinated to nine H_2O molecules and the Lu^{3+} ions were coordinated to eight [41] (Table S4). Due to the changes in the thermodynamic properties of H_2O residing inside the pores,[5, 54] the thermodynamic properties of the confined Ln^{3+} ions differ from the "standard" (unconfined) values. When Ln^{3+} ion resides in a confined domain, its ΔG_{hydr} becomes less negative (Table S4), which would make Ln^{3+} dehydration less energetically costly and therefore favor inner-sphere adsorption, in agreement with the pH trends from the batch adsorption experiments.

Conclusion

An ion's ΔG_{hydr} determines whether (and to what degree) nanoconfinement will change its adsorption energetics and coordination environment on a SiO_2 surface. Three chemical mechanisms could explain the observed shifts in the energetics and macroscopic adsorption trends due to nanoconfinement of the SiO_2- H_2O interface, either alone or in tandem: (1) nanoconfinement promotes inner-sphere complexation between Ln^{3+} ions and the SiO_2 surface; (2) nanoconfinement promotes the formation of polymeric Ln^{3+} species only on the surfaces of porous SiO_2 solids (not on non-porous SiO_2); (3) nanoconfinement makes the Ln^{3+} ΔG_{hydr} less negative, reducing the energy required to achieve a dehydration reaction and the formation of an inner-sphere surface complex. These proposed mechanisms are illustrated in Figure 6. Additionally, we observed that nanoconfinement causes a slight elongation of the Ln−O and

Ln−Si bond lengths for Ln^{3+} adsorbed onto the SiO_2 surface as an inner-sphere complex. The combination of these nanoconfinement effects on the interfacial chemical processes cumulatively result in a dramatic shift in the energetics of Ln^{3+} adsorption, causing the reaction to switch from an *endo*- to an *exothermic* process. In summary, nanoconfinement changes the energetics and products of interfacial reactions at the SiO_2-H_2O interface, and these effects are more pronounced for ions with lower hydration free energies.

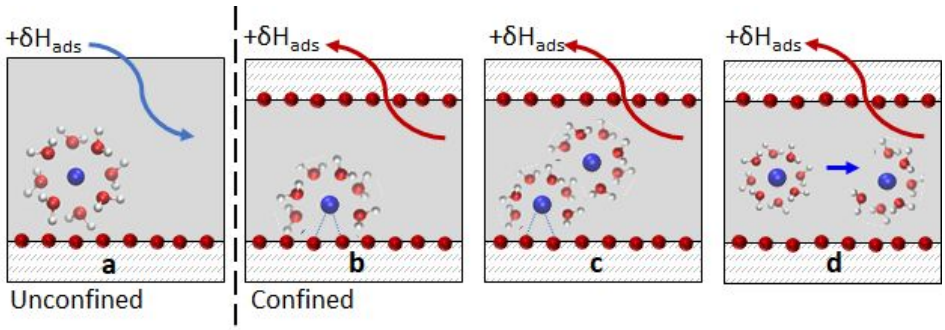

Figure 6. Proposed Ln^{3+} adsorption mechanisms which can result in an *endothermic* (+δH**)** or an *exothermic* (-δH**)** signal. (a) Ln^{3+} adsorption as an outer-sphere complex on unconfined SiO_2 surface; (b) Ln^{3+} adsorption as an inner-sphere complex on confined SiO_2 surface; (c) Ln^{3+} adsorption as an inner-sphere dimer complex on confined SiO_2 surface; (d) Decrease in ΔG_{hydr} under nanoconfinement, making dehydration reaction less energetically costly.

Acknowledgements

The authors thank Y. Ding for help during XAS data collection, P. Lu for aquiring TEM image included in the SI, and J. Greathouse for pre-submission review of this manuscript. This material is based upon work supported by the U.S. Department of Energy, Office of Science, Office of Basic Energy Sciences, Chemical Sciences, Geosciences, and Biosciences Division under contract DE-NA0003525. The experimental work was performed at Sandia National Laboratories. Sandia National Laboratories is a multimission laboratory managed and operated by National Technology and Engineering Solutions of Sandia LLC, a wholly owned subsidiary

of Honeywell International Inc., for the U.S. Department of Energy's National Nuclear Security Administration under contract DE-NA-0003525. X-ray Absorption Spectroscopy experiments were performed at Sector 10 at the Advanced Photon Source, an Office of Science User Facility operated for the U.S. Department of Energy (DOE) Office of Science by Argonne National Laboratory. This paper describes objective technical results and analysis. Any subjective views or opinions that might be expressed in the paper do not necessarily represent the views of the U.S. Department of Energy or the United States Government.

Conflicts of interest

The authors declare no competing interests.

Author contributions

AGI developed research hypothesis, performed batch adsorption and XAFS experiments and data analysis, and wrote the manuscript with input from the co-authors. PIK and NK performed microcalorimetry experiments and interpreted the data. KL performed DFT calculations and data analysis. AWK assisted with XAFS data collections, and LL assisted with bulk adsorption experiments.

Supporting Information Available

Supporting information includes transmission electron microscopy image of porous silica channels; Summary Table containing K_{ads} values calculated for competitive adsorption experiments; Summary Table of XAFS shell-by-shell fitting results; Summary Table of measured heats of adsorption in flow microcalorimetry experiments; and Calculated ΔG_{hydr} for

Nd^{3+} and Lu^{3+} as a function of dielectric constant of H_2O. This material is available free of charge.

References

1. A. G. Ilgen, J. E. Heath, I. Y. Akkutlu, L. T. Bryndzia, D. R. Cole, Y. K. Kharaka, T. J. Kneafsey, K. L. Milliken, L. J. Pyrak-Nolte and R. Suarez-Rivera, Shales at all scales: Exploring coupled processes in mudrocks, *Earth-Science Reviews*, 2017, **166**, 132-152.
2. Y. Wang, Nanogeochemistry: nanostructures, emergent properties and their control on geochemical reactions and mass transfers, *Chem. Geol.*, 2014, **378**, 1-23.
3. H. Blatt, R. Tracy and B. Owens, *Petrology: igneous, sedimentary, and metamorphic*, Macmillan, 2006.
4. W. H. Thompson, Perspective: Dynamics of confined liquids, *The Journal of chemical physics*, 2018, **149**, 170901.
5. E. Breynaert, M. Houlleberghs, S. Radhakrishnan, G. Grübel, F. Taulelle and J. A. Martens, Water as a tuneable solvent: a perspective, *Chem. Soc. Rev.*, 2020, **49**, 2557-2569.
6. I. Brovchenko and A. Oleinikova, *Interfacial and confined water*, Elsevier, 2008.
7. S. Singh, J. Houston, F. van Swol and C. J. J. N. Brinker, Superhydrophobicity: drying transition of confined water, 2006, **442**, 526.
8. Y. Wang, C. Bryan, H. Xu and H. Gao, Nanogeochemistry: Geochemical reactions and mass transfers in nanopores, *Geology*, 2003, **31**, 387-390.
9. A. W. Knight, P. Ilani-Kashkouli, J. A. Harvey, J. A. Greathouse, T. A. Ho, N. Kabengi and A. G. Ilgen, Interfacial reactions of Cu (ii) adsorption and hydrolysis driven by nano-scale confinement, *Environmental Science: Nano*, 2020.
10. J. Nelson, J. R. Bargar, L. Wasylenki, G. E. Brown Jr and K. Maher, Effects of nano-confinement on Zn (II) adsorption to nanoporous silica, *Geochim. Cosmochim. Acta*, 2018, **240**, 80-97.
11. D. Ferreira and C. Schulthess, The nanopore inner sphere enhancement effect on cation adsorption: Sodium, potassium, and calcium, *Soil Science Society of America Journal*, 2011, **75**, 389-396.
12. A. Phan, D. R. Cole and A. Striolo, Factors governing the behaviour of aqueous methane in narrow pores, *Phil. Trans. R. Soc. A*, 2016, **374**, 20150019.
13. J. P. Thiruraman, P. Masih Das and M. Drndić, Ions and Water Dancing through Atom-Scale Holes: A Perspective toward "Size Zero", *ACS nano*, 2020, **14**, 3736-3746.
14. D. Argyris, D. R. Cole and A. Striolo, Ion-specific effects under confinement: the role of interfacial water, *Acs Nano*, 2010, **4**, 2035-2042.
15. G. Rother, A. G. Stack, S. Gautam, T. Liu, D. R. Cole and A. Busch, Water Uptake by Silica Nanopores: Impacts of Surface Hydrophilicity and Pore Size, *The Journal of Physical Chemistry C*, 2020, **124**, 15188-15194.
16. T. Takei, K. Mukasa, M. Kofuji, M. Fuji, T. Watanabe, M. Chikazawa and T. Kanazawa, Changes in density and surface tension of water in silica pores, *Colloid. Polym. Sci.*, 2000, **278**, 475-480.

17. L. Fumagalli, A. Esfandiar, R. Fabregas, S. Hu, P. Ares, A. Janardanan, Q. Yang, B. Radha, T. Taniguchi and K. Watanabe, Anomalously low dielectric constant of confined water, *Science*, 2018, **360**, 1339-1342.
18. S. Kittaka, S. Ishimaru, M. Kuranishi, T. Matsuda and T. Yamaguchi, Enthalpy and interfacial free energy changes of water capillary condensed in mesoporous silica, MCM-41 and SBA-15, *PCCP*, 2006, **8**, 3223-3231.
19. S. Senapati and A. Chandra, Dielectric constant of water confined in a nanocavity, *The Journal of Physical Chemistry B*, 2001, **105**, 5106-5109.
20. S. Le Caër, S. Pin, S. Esnouf, Q. Raffy, J. P. Renault, J.-B. Brubach, G. Creff and P. Roy, A trapped water network in nanoporous material: the role of interfaces, *PCCP*, 2011, **13**, 17658-17666.
21. G. H. Findenegg, S. Jähnert, D. Akcakayiran and A. Schreiber, Freezing and melting of water confined in silica nanopores, *ChemPhysChem*, 2008, **9**, 2651-2659.
22. F. X. Coudert, R. Vuilleumier and A. Boutin, Dipole moment, hydrogen bonding and IR spectrum of confined water, *ChemPhysChem*, 2006, **7**, 2464-2467.
23. A. W. Knight, A. Tigges and A. Ilgen, Adsorption of Copper on Mesoporous Silica: The Effect of Nano-scale Confinement, *Geochem. Trans.*, 2018.
24. D. Wu and A. Navrotsky, Small molecule–Silica interactions in porous silica structures, *Geochim. Cosmochim. Acta*, 2013, **109**, 38-50.
25. S. H. Chen, F. Mallamace, L. Liu, D. Liu, X. Chu, Y. Zhang, C. Kim, A. Faraone, C. Y. Mou and E. Fratini, 2008.
26. R. K. Kalluri, D. Konatham and A. Striolo, Aqueous NaCl solutions within charged carbon-slit pores: Partition coefficients and density distributions from molecular dynamics simulations, *The Journal of Physical Chemistry C*, 2011, **115**, 13786-13795.
27. M. S. Sansom and P. C. Biggin, Biophysics: water at the nanoscale, *Nature*, 2001, **414**, 156-159.
28. D. Mattia and F. Calabrò, Explaining high flow rate of water in carbon nanotubes via solid–liquid molecular interactions, *Microfluidics and nanofluidics*, 2012, **13**, 125-130.
29. A. R. Zimmerman, J. Chorover, K. W. Goyne and S. L. Brantley, Protection of mesopore-adsorbed organic matter from enzymatic degradation, *Environmental Science & Technology*, 2004, **38**, 4542-4548.
30. D. Ferreira, C. Schulthess and N. Kabengi, Calorimetric evidence in support of the nanopore inner sphere enhancement theory on cation adsorption, *Soil Science Society of America Journal*, 2013, **77**, 94-99.
31. H. B. Jung, M. I. Boyanov, H. Konishi, Y. Sun, B. Mishra, K. M. Kemner, E. E. Roden and H. Xu, Redox behavior of uranium at the nanoporous aluminum oxide-water interface: Implications for uranium remediation, *Environmental science & technology*, 2012, **46**, 7301-7309.
32. S. Patra, A. K. Pandey, S. K. Sarkar and A. Goswami, Wonderful nanoconfinement effect on redox reaction equilibrium, *RSC Advances*, 2014, **4**, 33366-33369.
33. S. Patra, A. K. Pandey, D. Sen, S. V. Ramagiri, J. R. Bellare, S. Mazumder and A. Goswami, Redox Decomposition of Silver Citrate Complex in Nanoscale Confinement: An Unusual Mechanism of Formation and Growth of Silver Nanoparticles, *Langmuir*, 2014, **30**, 2460-2469.

34. Y. Suzuki, H. Duran, M. Steinhart, M. Kappl, H.-J. r. Butt and G. Floudas, Homogeneous nucleation of predominantly cubic ice confined in nanoporous alumina, *Nano Lett.*, 2015, **15**, 1987-1992.
35. M. V. Massa, M. S. Lee and K. Dalnoki‐Veress, Crystal nucleation of polymers confined to droplets: Memory effects, *J. Polym. Sci., Part B: Polym. Phys.*, 2005, **43**, 3438-3443.
36. Q. Jiang and M. D. Ward, Crystallization under nanoscale confinement, *Chem. Soc. Rev.*, 2014, **43**, 2066-2079.
37. V. Monnier, N. Sanz, E. Botzung-Appert, M. Bacia and A. Ibanez, Confined nucleation and growth of organic nanocrystals in sol–gel matrices, *J. Mater. Chem.*, 2006, **16**, 1401-1409.
38. A. G. Stack, A. Fernandez-Martinez, L. F. Allard, J. L. Bañuelos, G. Rother, L. M. Anovitz, D. R. Cole and G. A. Waychunas, Pore-size-dependent calcium carbonate precipitation controlled by surface chemistry, *Environmental science & technology*, 2014, **48**, 6177-6183.
39. Q. R. Miller, J. P. Kaszuba, H. T. Schaef, M. E. Bowden, B. P. McGrail and K. M. Rosso, Anomalously low activation energy of nanoconfined MgCO 3 precipitation, *Chem. Commun.*, 2019, **55**, 6835-6837.
40. P. D'Angelo and R. J. C. A. E. J. Spezia, Hydration of lanthanoids (III) and actinoids (III): an experimental/theoretical saga, 2012, **18**, 11162-11178.
41. J. Zhang, N. Heinz and M. J. I. c. Dolg, Understanding lanthanoid (III) hydration structure and kinetics by insights from energies and wave functions, 2014, **53**, 7700-7708.
42. N. Krishnamurthy and C. K. Gupta, *Extractive metallurgy of rare earths*, CRC press, 2004.
43. B. Ravel and M. Newville, ATHENA, ARTEMIS, HEPHAESTUS: data analysis for X-ray absorption spectroscopy using IFEFFIT, *Journal of Synchrotron Radiation*, 2005, **12**, 537-541.
44. M. Newville, IFEFFIT: interactive XAFS analysis and FEFF fitting, *Journal of Synchrotron Radiation*, 2001, **8**, 322-324.
45. M. Newville, P. Livins, Y. Yacoby, J. Rehr and E. Stern, Near-edge x-ray-absorption fine structure of Pb: A comparison of theory and experiment, *Physical Review B*, 1993, **47**, 14126-14131.
46. S. Kelly, D. Hesterberg and B. Ravel, in *Methods of Soil Analysis: Part 5--Mineralogical Methods*, eds. A. Ulery and L. Drees, Soil Science Society of America, Madison, WI, USA, 2008, ch. 14, pp. 387-465.
47. S. Zabinsky, J. Rehr, A. Ankudinov, R. Albers and M. Eller, Multiple-scattering calculations of x-ray-absorption spectra, *Physical Review B*, 1995, **52**, 2995-3009.
48. M. E. Fleet and Y. Pan, Site preference of rare earth elements in fluorapatite, *Am. Mineral.*, 1995, **80**, 329-335.
49. R. Rhue, C. Appel and N. Kabengi, Measuring surface chemical properties of soil using flow calorimetry 1, *Soil science*, 2002, **167**, 782-790.
50. M. Frisch, G. Trucks, H. Schlegel, G. Scuseria, M. Robb, J. Cheeseman, G. Scalmani, V. Barone, B. Mennucci and G. Petersson, Gaussian, Inc., Wallingford CT, *Gaussian 09*, 2009.

51. G. Scalmani and M. J. Frisch, Continuous surface charge polarizable continuum models of solvation. I. General formalism, *The Journal of chemical physics*, 2010, **132**, 114110.
52. T. R. Cundari and W. J. Stevens, Effective core potential methods for the lanthanides, *The Journal of chemical physics*, 1993, **98**, 5555-5565.
53. D. S. Jordan, J. N. Malin and F. M. Geiger, Interactions of Al (III), La (III), Gd (III), and Lu (III) with the fused silica/water interface studied by second harmonic generation, *Environmental science & technology*, 2010, **44**, 5862-5867.
54. A. W. Knight, N. G. Kalugin, E. Coker and A. G. Ilgen, Water properties under nano-scale confinement, *Scientific reports*, 2019, **9**, 8246.
55. V. S. Bryantsev, M. S. Diallo, A. C. Van Duin and W. A. Goddard III, Hydration of copper (II): new insights from density functional theory and the COSMO solvation model, *The Journal of Physical Chemistry A*, 2008, **112**, 9104-9112.
56. Y. Ni, J. M. Hughes and A. N. Mariano, Crystal chemistry of the monazite and xenotime structures, *Am. Mineral.*, 1995, **80**, 21-26.
57. O. Yakubovich, M. Simonov, A. Voloshin and Y. Pakhomovsky, Crystal structure of keivite Yb2[Si2O7], *Soviet Physics Doklady*, 1986, **31**, 930-932.
58. W. Piasecki and D. A. Sverjensky, Speciation of adsorbed yttrium and rare earth elements on oxide surfaces, *Geochim. Cosmochim. Acta*, 2008, **72**, 3964-3979.
59. S. S. Lee, P. Fenter, K. L. Nagy and N. C. Sturchio, Changes in adsorption free energy and speciation during competitive adsorption between monovalent cations at the muscovite (0 0 1)-water interface, *Geochim. Cosmochim. Acta*, 2013, **123**, 416-426.
60. V. Bakaev, T. Bakaeva and C. G. Pantano, On inverse adsorption chromatography. 2. Determination of isotherms and heats of adsorption as well as energy distributions of adsorption sites, *The Journal of Physical Chemistry C*, 2007, **111**, 7473-7486.
61. P. Grabowski, D. Riccardi, M. A. Gomez, D. Asthagiri and L. R. Pratt, Quasi-chemical theory and the standard free energy of H+ (aq), *The Journal of Physical Chemistry A*, 2002, **106**, 9145-9148.